ACS OMEGA

Article

Cite This: ACS Omega 2019, 4, 1130−1138

http://pubs.acs.org/journal/acsodf

Polyaniline-Layered Rutile TiO_2 Nanorods as Alternative Photoanode in Dye-Sensitized Solar Cells

Anurag Roy,[†,‡,#] Soumita Mukhopadhyay,[†,§,#] Parukuttyamma Sujatha Devi,[*,†] and Senthilarasu Sundaram[‡]

[†]Sensor and Actuator Division, CSIR-Central Glass and Ceramic Research Institute, Kolkata 700032, India

[‡]Environment and Sustainability Institute, University of Exeter, Penryn, Cornwall TR10 9FE, United Kingdom

Supporting Information

ABSTRACT: In this paper, dye-sensitized solar cell (DSSC) performance of the less explored polymorph of TiO_2, rutile, has been explored, and its performance has been modified with polyaniline (PANI) wrapping on the surface. For this purpose, highly crystalline rutile nanorods have been synthesized without any growth-directing substrates, employing a hydrothermal treatment. Further, to understand the phase composition and morphology, the synthesized nanorods and PANI-layered nanorods have been characterized through various physicochemical methods. The synthesized rods were implemented as photoanode material for DSSCs which exhibited a photoelectric conversion efficiency (PCE) of 4.28% with a high open-circuit voltage (V_{OC}) of 0.84 V which is highly superior to DSSC with Degussa P25 (PCE = 3.95%) TiO_2 nanoparticles. The resultant PCE of the nanorods was further enhanced to 6.23% on *in situ* deposition of PANI which acts as an electron-transporting layer. Introduction of conducting PANI over the rutile rod was explored as a new concept to improve the performance of photoanode material besides conventional $TiCl_4$ treatment or scattering layer deposition.

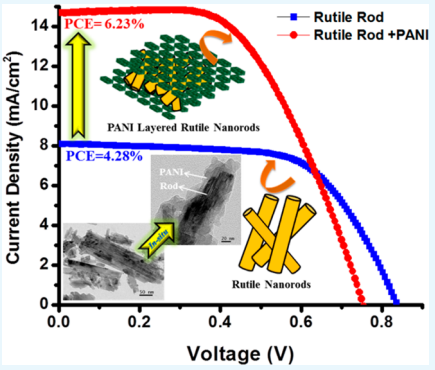

INTRODUCTION

Of late, there has been a great impetus to design and develop functional nanomaterials for energy-harvesting applications. Among various existing technologies, simple construction and low cost have stimulated great research interest in dye-sensitized solar cells (DSSCs).[1−3] Since 1991, after the first breakthrough in DSSCs reported by O'Regan and Grätzel, TiO_2 has been identified as the state of the art photoanode material due to its impressive performance.[4] We have been working on various oxide materials to identify new photoanodes for DSSCs. In this direction, various metal oxides such as TiO_2, ZnO, Zn_2SnO_4, and $BaSnO_3$ have been explored as potential photoanode materials in DSSCs.[5−8] Remarkable efforts have been endeavored to establish effective performance of TiO_2 by better synthesis techniques, phase growth, tuning of morphology, band gap alignment, doping, making composites, etc. for various applications. It is worth mentioning that the properties and performance of TiO_2 strictly depend on its crystallographic phase, morphological pattern, dimensions, and surface properties.[1,2,9] Among the three main crystallographic phases of TiO_2, such as anatase, rutile, and brookite, numerous pioneering reports highlighted the superior performance of anatase TiO_2 as compared to rutile or a less stable brookite crystal pattern mainly in photovoltaic or photocatalytic applications.[10−16] On the contrary, the excellent performance of mixed-phase materials, namely, Degussa P25 (commercial TiO_2), compared to single-phase anatase TiO_2 cannot be ruled out which eventually prompted us to explore the performance of rutile TiO_2 rather than a conventional anatase photoanode. Rutile TiO_2 is often neglected in many applications compared to the anatase phase due to several of its unfavorable properties: high-temperature synthesis technique adopted to produce rutile TiO_2 leads to unavoidable aggregation of the nanocrystals which exerts lower dye loading capacity and lower charge diffusion coefficient. More positive conduction band edge potential compared to anatase also declines electron transport capacity, though there are few controversial reports related to the position of conduction band edge in rutile TiO_2.[17,18] On the other hand, compared to anatase, the rutile has striking advantages like more chemical stability and effective light-scattering capacity owing to its higher refractive index.[19−21] Hence, in recent years, tailoring rutile TiO_2 to enable it as an alternative photoanode to anatase polymorph in DSSCs has become an interesting area of research.[22−31] Among various morphological patterns, one-dimensional (1D) nanorods or nanowires have distinctive physicochemical properties in comparison to random nanoparticles.[9] The overall conversion efficiency of nanoparticles is restricted due to percolation of charge carriers through grain boundaries, resulting in higher recombination. On the other hand, when nanorods/nanowires are employed as photoanode in DSSC applications, their one-dimensional morphology with high

Received: October 2, 2018
Accepted: December 18, 2018
Published: January 14, 2019

DOI: 10.1021/acsomega.8b02628
ACS Omega 2019, 4, 1130−1138

aspect ratio efficiently transports conduction electrons through a direct central conducting pathway and prevents recombination in the radial direction. The overall energy conversion efficiency of DSSCs has been decided by the competition between the electron transport efficiency through photoanode and recombination of electrons with electrolytes on the semiconductor electrolyte interface. A photoanode comprised of 1D morphology exerts superior performance over nanoparticles like counterparts.[32−34] In this paper, we have synthesized rutile nanorods via a low-temperature hydrothermal process to bypass the disadvantages. Additionally, its one-dimensional morphology with high aspect ratio efficiently transports conduction electrons through a direct central conducting pathway and prevents recombination in the radial direction which eventually exhibits superior efficiency even compared to P25.[10,19,24,29,33] In our earlier studies, we have demonstrated a better performance for ZnO rods or fiber-like structures of various other photoanode oxide materials as compared to other morphologies.[5,8,35−37] Rutile TiO_2 rods exhibit better chemical stability and performance as a stable photoanode in DSSCs. Out of very rare reports describing the hydrothermally processed rutile nanorods, in most of the cases FTO has been used as substrates to grow 1D morphology followed by post treatment with $TiCl_4$ to achieve better efficiency in DSSCs.[29,30,32,34] For example, Liu et al. (2009) reported 3% power conversion efficiency of single crystalline rutile nanorods after modification with $TiCl_4$.[38] Lv et al. (2012, 2013) fabricated densely aligned rutile nanorod arrays using FTO substrate and achieved a power conversion efficiency of 1.3%, whereas in another report an efficiency of 2.35% has been reported for unetched TiO_2 nanorods.[29,31] Template-free or surfactant-free growth of rod morphology pose a serious challenge to develop pure TiO_2 rutile materials. We have discovered a facile way to create rod structure by variation of reaction pH and also by avoiding the usage of surfactants, structure-directing agents, and/or metal−organic templates. On the other hand, the well-studied conducting polymer, polyaniline (PANI), has been widely used as an active component for the photocatalytic, photovoltaic, and photoelectrochemical device fabrication owing to its unique electrical properties, easy preparation methods, and eco-friendly nature.[39−41] In addition, the conjugated structure of PANI can capture more photoelectrons, which in turn can retard the recombination between photoexcitons. Moreover, the performance of PANI augments the visible-light absorption and thereby produces more photoelectrons under solar irradiation. Consequently, it has been thought of worthwhile to implement PANI as an active component in DSSC devices. There are several reports using PANI as an active component in photocatalytic application and as an alternative counter electrode for DSSC fabrication.[42−44] The PANI-hybridized metal oxide semiconductor has also been reported to enhance the efficiency of electron separation and suppress the photocorrosion.[45,46] To improve the optical absorption of the incident light, an additional overlayer on the nanocrystalline TiO_2 photoanode will enhance the light scattering in DSSCs. Besides, functional materials having both superior light-scattering properties and high surface area are also being treated in DSSCs to improve the incident light absorption.[47,48] As a new concept, electron-transporting layer insertions can be explored as another way to enhance the efficiency of the photoanode. In this work, the TiO_2 rutile rod has been employed as a photoanode, which exhibited an overall conversion efficiency of 4.28%, which is higher than the commercially available anatase-based TiO_2, Degussa-P25 (3.95%), using N719 dye as a photosensitizer. Furthermore, cloaking the rutile nanorod with PANI layers enhanced the conversion efficiency to 6.23%. An underlying phenomenon for this superior performance was thoroughly investigated and discussed in the following sections. To the best of our knowledge, for the first time we coupled rutile nanorods with PANI as a photoanode in DSSCs as a means to improve the performance of the cell.

RESULTS AND DISCUSSION

In order to investigate the phase purity of the as-prepared powder, the powder X-ray diffraction (XRD) technique was carried out. Figure 1a shows the XRD pattern of bare TiO_2

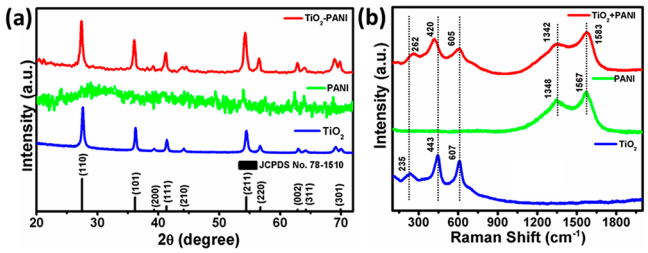

Figure 1. (a) X-ray diffraction pattern and (b) Raman spectra of rutile TiO_2, PANI, and PANI−TiO_2 samples, respectively.

nanorod, PANI and PANI deposited TiO_2. The patterns show that the diffraction peaks of synthesized powder resembles with the crystal structure of rutile phase of TiO_2 (JCPDS card no.-78−1510). It is interesting to note here that XRD pattern for PANI deposited TiO_2 rod sample is almost similar to that of bare TiO_2 rod sample. The absence of any significant peak of PANI in the film may be due to the lower degree of crystallization of PANI. Raman spectroscopic analysis was also performed in order to understand the phase formation of synthesized TiO_2 and PANI inserted TiO_2, as shown in Figure 1b. The characteristic sharp Raman bands of TiO_2 sample at 443 (E_g) and 607 cm^{-1}(A_{1g}) and a second-order phonon (235 cm^{-1}) were recognized for rutile phase of TiO_2. In addition, peaks appeared at 1348 and 1567 cm^{-1} belonging to the G and D band of the PANI structure. The I_D/I_G ratio of 0.856 confirms the graphitic nature of the deposited PANI. The case of the PANI-deposited TiO_2 sample exhibited characteristic peaks of rutile TiO_2 and PANI simultaneously with a significant shifting of the peak compared to their bare form. This is indicative of deposition of PANI leading to interaction with TiO_2 at the surface, resulting in displacement of their characteristic Raman peaks.

Further, the FTIR spectra interpretation also confirms the successful PANI deposition over TiO_2 as shown in Figure. 2a. The weaker vibrational modes at ∼1313 and 1140 cm^{-1} represent the C−N stretching frequency for the aromatic amine nitrogen, and the amine nitrogen−quinoid ring of the polymeric structure of PANI exhibited a blue shift, respectively. This result interprets that a widely conjugated system containing PANI and TiO_2 had formed. The broad band in Figure 2a centered at ∼3446 cm^{-1} corresponds to the stretching frequency of hydroxyl bonds of adsorbed water on the TiO_2 surface which is significantly reduced after deposition of PANI. This may be due to the presence of labile surface hydroxyl groups which are mainly responsible for the PANI

DOI: 10.1021/acsomega.8b02628
ACS Omega 2019, 4, 1130−1138

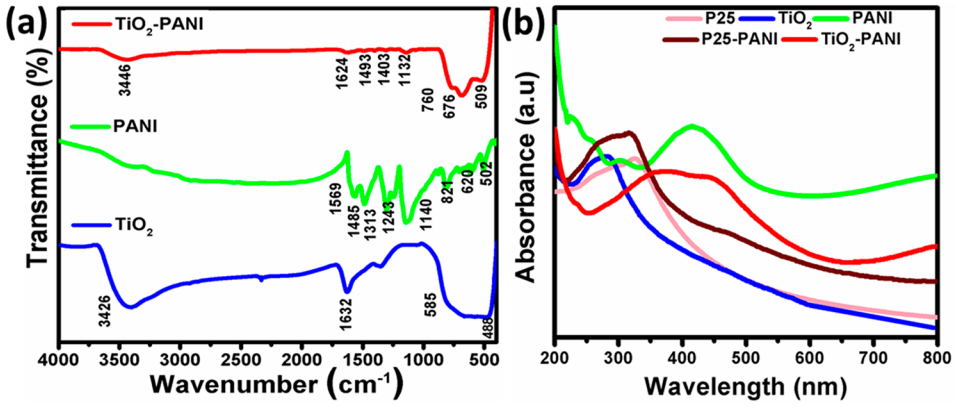

Figure 2. (a) FTIR spectra of synthesized rutile TiO_2, PANI, and PANI−TiO_2 and (b) UV−vis spectra of P25, P25−PANI, synthesized rutile TiO_2, bare PANI, and PANI−TiO_2.

deposition over the surface of the TiO_2. The sharp and intense band appeared at 585 and 480 cm^{-1} assigned to the characteristic vibration band for Ti−O−Ti of the rutile structure of the bond vibration. Figure 2b indicates the UV−vis absorption spectra of the same sample which exhibits a significant bathochromic shift but resulted in a wide band between 300 and 600 nm. The absorption band of bare PANI observed at ∼440 nm indicates leading visible absorption compared to rutile TiO_2 (∼300 nm). Therefore, all the above analyses strongly recommend successful deposition of PANI over the bare TiO_2 surface. The UV−vis absorption spectra of the rutile rod TiO_2−PANI composite samples exhibited a broad band between 300 and 600 nm with a significant bathochromic shift compared to the absorbance of the corresponding single-phase materials. Compared to this, the P25−PANI composite exhibits a maximum absorption at ∼320 nm with a weak absorption at ∼462 nm (Figure 2b). The TEM bright field reveals a randomly directed particle−PANI composite distribution which could affect the absorption peak and retain the distinct P25 absorption peak even after the composite formation (Figure 3). In contrast, perfect wrapping of rutile nanorods by the PANI layer augmented the appearance of a broad band between 300 and 600 nm and exhibited a significant bathochromic shift compared to rutile TiO_2 and PANI (Figure 2b).

Further, the morphology of the TiO_2 sample was investigated in detail by transmission electron microscopy (TEM) and high-resolution transmission electron microscopy (HRTEM) as shown in Figure 3a,b. The bright-field image of as-synthesized TiO_2 exhibited densely packed elongated nanorods with a length of 300−350 nm and an average width of 13 ± 2 nm as shown in Figure 3a,b. From Figure 3a, it appeared like these rods were laterally self-assembled to form a bundle-like pattern. In each bundle similar types of nanorods are tightly held together. The highly crystalline nature of individual nanorods can be easily observed from the HRTEM images shown in Figure 3c. Two sets of lattice fringes perpendicular to each other with distances of 0.29 and 0.32 nm can be readily observed corresponding to the *d* spacings of (001) and (110) reflections of rutile TiO_2. It was observed that the nanorods preferentially expose the {110} low energy facets and grow along the [001] direction. Here, Cl^- plays a vital role in the growth of TiO_2 grains into nanorods instead of nanoparticles. The Cl^- is selectively adsorbed onto the positive polar face of the rutile {110} planes which restrict the

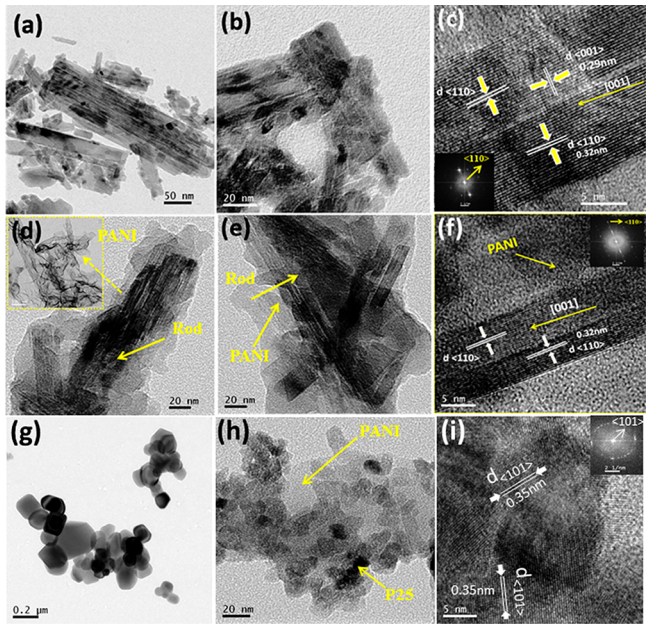

Figure 3. TEM bright-field image of (a),(b) rutile TiO_2 nanorod, (d), (e) rutile TiO_2 nanorod−PANI composite at different magnification, respectively. HRTEM image of (c)−(f) rutile TiO_2 nanorod and nanorod TiO_2−PANI composite (inset: corresponding FFT pattern), respectively. Bright-field image of (g) P25, (h) P25−TiO_2 composite sample, and (i) HRTEM image of P25−TiO_2 composite (inset: corresponding FFT pattern).

coalescence of TiO_2 grains on this surface and accelerate the growth along the [001] direction, resulting in the growth of rutile nanorods instead of nanoparticles. TEM studies on the PANI−TiO_2 indicate unflinching wrapping of PANI on the TiO_2 nanorods as shown in Figure 3d,e. Figure 3d (inset) depicts the sheet-like layer texture of the PANI which was rationally deposited onto the nanorods to form a PANI−TiO_2 composite. Figure 3f exhibits the corresponding HRTEM image and the FFT pattern at the inset. This interfacial contact is beneficial for photoelectron transport to improve its performance in DSSCs. Each bundle of nanorods possesses approximately close dimension of rods, and the aspect ratio varies between 20 ± 5 as observed from TEM analysis. Alike rods are laterally self-assembled to form a bundle-like pattern, and in each bundle they are tightly held together as they are synthesized without any structure-directing agent or surfactant.

DOI: 10.1021/acsomega.8b02628
ACS Omega 2019, 4, 1130−1138

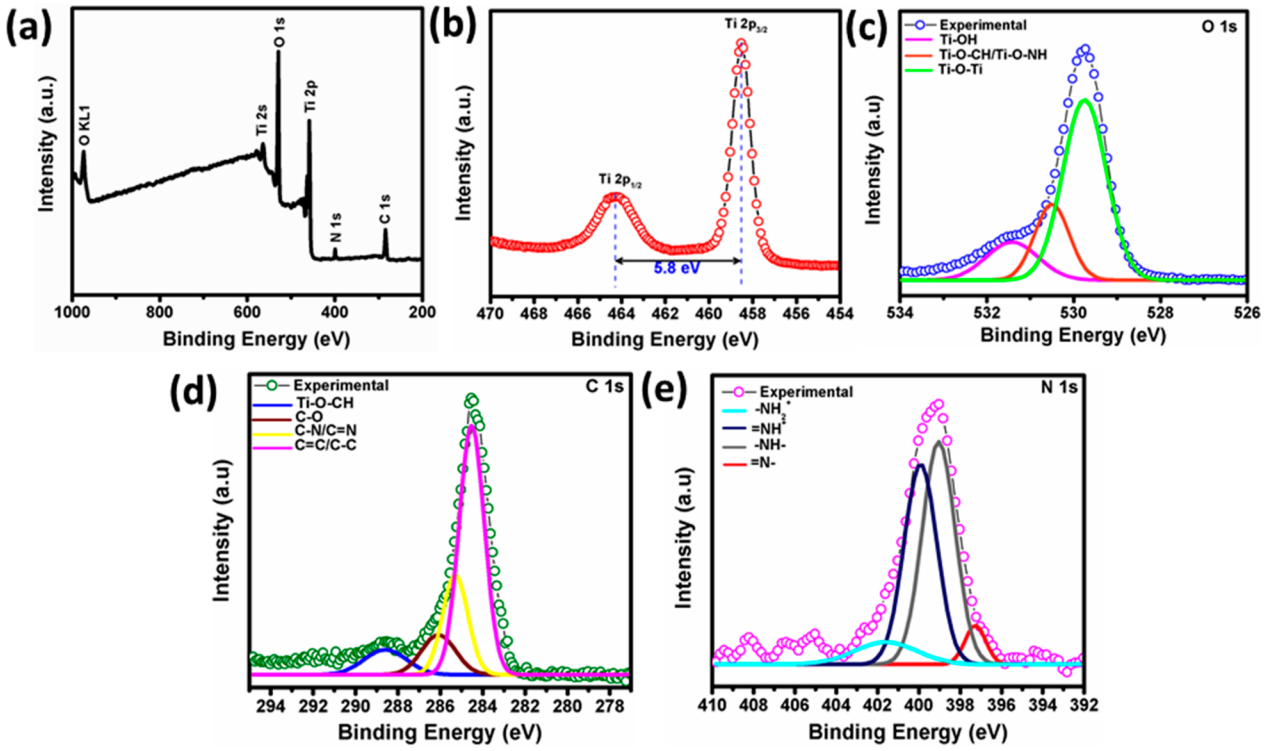

Figure 4. (a) XPS survey and core level spectrum of (b) Ti 2p, (c) O 1s, (d) C 1s, and (e) N 1s of TiO_2−PANI composite film.

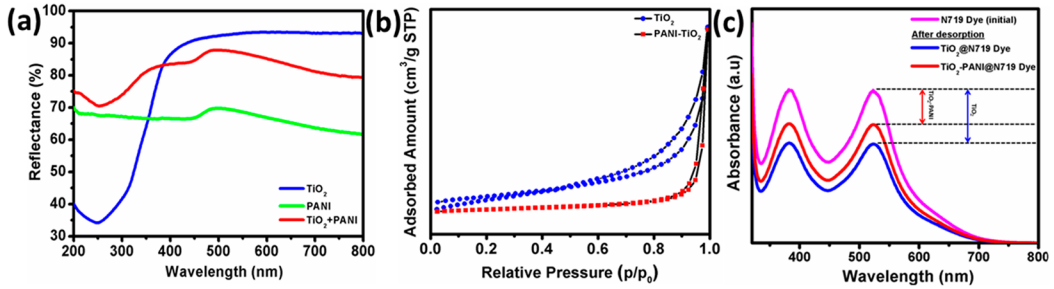

Figure 5. (a) DR spectra of the TiO_2 nanorod, PANI, and PANI-deposited TiO_2 sample, (b) BET surface area plot of TiO_2 nanorod and PANI-deposited TiO_2 samples, and (c) UV−Vis absorption spectra of initial N719 dye and remaining N719 dye after adsorption on TiO_2 and TiO_2−PANI films, respectively.

PANI deposited through an *in situ* process onto the rutile nanorods wrapped on the 1D surface without compromising rod dimensions and crystallinity as observed from the TEM images. A bright-field image of the P25 sample was given in Figure 3g. Besides, PANI deposition was also carried out for the P25 sample, and the corresponding bright-field image was given in Figure 3h. Figure 3i shows the corresponding HRTEM image, and the FFT pattern at the inset indicates the ⟨101⟩ plane having an interplanner distance of 0.35 nm which represents the anatase phase of the P25 sample.

A thorough X-ray photoelectron spectroscopy (XPS) analysis of the PANI-deposited rutile rod film was undertaken in order to find the chemical state of the elements present in PANI and TiO_2. Figure 4a exhibits the survey spectrum of the PANI-deposited rutile rod film. The presence of TiO_2 and PANI can be ascertained by observing the binding energy of the Ti 2p, O 1s, C 1s, and N 1s core-level XPS spectrum as shown in Figure 4b−e. The XPS peaks at 464.6 and 458.8 eV shown in Figure 4b are attributed to the binding energies of Ti $2p_{1/2}$ and Ti $2p_{3/2}$ states with a spin−orbit separation of 5.8 eV, confirming the presence of characteristic Ti^{4+} in the sample. Figure 4c represents the high-resolution O 1s spectrum. By deconvolution, the observed three peaks correspond to Ti−O−Ti (530.1 eV), Ti−O−NH/Ti−O−CH (530.5 eV), and Ti−O−H (531.5 eV), respectively.[14] The carbon signal of the PANI-modified surface of TiO_2 comprises four components at 284.4, 285.3, 286.1, and 288.6 eV as shown in Figure 4d, corresponding to aromatic C═C/C−C, C−N/C═N, C−O, and Ti−O−CH bonding, respectively. The peaks at 401.7, 399.9, 399, and 397.2 eV in the XPS core level spectrum of N 1s correspond to protonated amine ($-NH_2^+$), protonated imine (═NH^+), amine (−NH−), and imine (═N−) groups, respectively, as originated from the emeraldine form of PANI. This indicates successful formation of PANI during the *in situ* preparation as shown in Figure 4(e). Throughout the XPS spectrum analysis it has been observed that the bonding between TiO_2 and PANI has been attributed to hydrogen bonding and electrostatic interaction as evident from the core level peaks appearing at 530.5 and 288.6 eV due to significant bonding interaction of Ti−O−NH/Ti−O−CH

DOI: 10.1021/acsomega.8b02628
ACS Omega 2019, 4, 1130−1138

and Ti−O−CH during *in situ* deposition of PANI to TiO_2. Thus, XPS study of TiO_2−PANI film also explores the intrinsic composite formation between TiO_2 and PANI with chemical interaction.[49,50]

While studying the diffuse reflectance (DR) spectrum, an interesting phenomenon was observed as shown in Figure 5a. The rutile TiO_2 nanorod exhibits ∼40% reflectance corresponding to ∼300 nm wavelength due to its 1D nanostructure, whereas deposition of PANI reduced the extent of reflectance, extending the wavelength toward the visible region. This result strictly confirms the wrapping of the amorphous PANI layer on crystalline TiO_2 rods, resulting in significant loss in reflectance. A weak broad reflectance was also observed in the case of bare PANI at ∼440 nm. However, it is noteworthy to mention that deposition of PANI onto TiO_2 nanorods improves its solar light-harvesting capacity by extending the wavelength region which is benevolent for DSSC application. In order to ascertain the effect of PANI incorporation to develop the TiO_2−PANI composite, the surface area and porosity measurements were executed for native TiO_2 and TiO_2−PANI samples (Figure 5(b)). BET-specific surface area analysis of synthesized TiO_2 and PANI-deposited TiO_2 samples revealed a surface area of 56.64 and 49.62 m^2/g, respectively, as shown in Figure 5b and Table S1. As evident from Figure 5b, the type IV isotherm with a hysteresis loop indicates the mesoporous characteristics of rutile rods. A minor decrease in the surface area was observed in the case of a PANI-deposited TiO_2 sample with a change in the adsorption isotherm from type IV to type III with mesoporous characteristics. Because of the comparatively high surface area of the synthesized TiO_2, it could adsorb a larger number of dye molecules on the surface than PANI-deposited TiO_2. All the characterization results support the successful deposition of PANI onto the TiO_2 surface.

In order to study the dye absorbing capability of the prepared samples, the UV−Vis absorption experiments were carried out as shown in Figure 5c. The UV−Vis absorption spectra of the residual dye solution collected after 24 h adsorption on both the TiO_2 and TiO_2−PANI films are presented in Figure 5c. The characteristic intensity of the residual N719 dye solution at 380 and 525 nm appeared lower for TiO_2 film than TiO_2−PANI film. The amounts of dye adsorbed per device active area and number of dye molecules attached with TiO_2 surface were also estimated by using the absorption spectra given in Table S1. The dye loading capability is also related to the surface area and porosity of the sample. Therefore, due to deposition of the PANI layer on the surface of the rutile rods, the surface area becomes lesser as evident from Figure 5b, resulting in lesser amount of dye loading leading to lesser fill factor than bare rutile rods.

Prior to investigating the photovoltaic performance, the FESEM microstructural investigation was carried out for TiO_2 and PANI-deposited TiO_2 films, as shown in Figure 6a,c. The FESEM cross-sectional microstructural image of the nanorod-based film exhibited rough surface of the rod samples as shown in Figure 6b,d, and the corresponding thickness was found to be ∼8.56 and 8.95 μm, respectively. The microstructural analysis reveals that the electrodes are of nearly uniform thickness which is an important criterion to exert high efficiency in DSSC performance. Furthermore, FESEM-EDAX elemental color mapping was also carried out and aimed to be a suitable technique to validate the presence of PANI onto the TiO_2 as shown for the TiO_2−PANI film as shown in Figure 6c. It shows the coexistence of Ti, C, N, and O belonging to PANI and TiO_2, respectively. This result further confirms the deposition of PANI onto the TiO_2 surface.

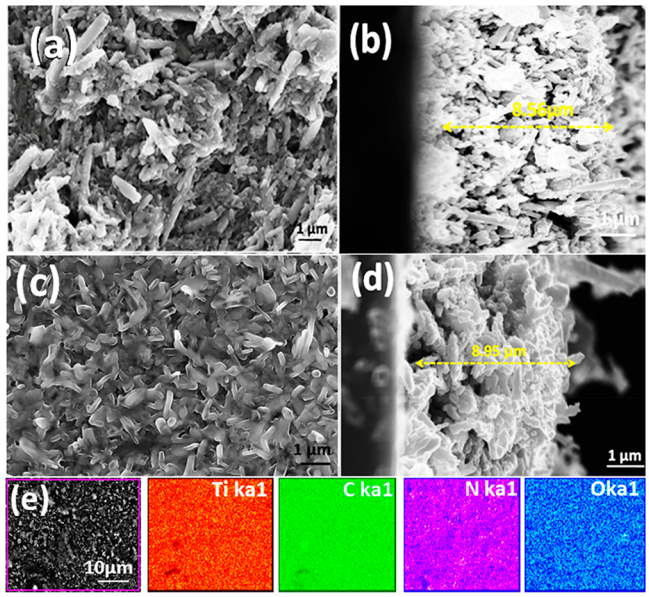

Figure 6. Microstructural and cross-sectional FESEM images of (a,b) bare TiO_2 and (c,d) PANI-deposited TiO_2, respectively, and (e) EDAX color elemental mapping for the following elements: Ti, O, C, and N of PANI-deposited TiO_2 film.

PHOTOVOLTAIC APPLICATION

The photovoltaic performance of both samples was compared as shown in Figure 7a,b. The transient photocurrent response was further investigated which exhibits higher current density in the case of TiO_2−PANI film compared to the respective bare forms for several cycles with the on−off pulse duration of 10 s, as exhibited in Figure 7a. This may further indicate that illumination of light can lead to photocurrent enhancement of TiO_2−PANI film compared to the respective bare form which indicates deposition of PANI. A comparative plot of J−V characteristics for bare rutile TiO_2 and PANI-coated film along with the commercial Degussa P25 TiO_2 is shown in Figure 7b, and their photovoltaic parameters are summarized in Table 1. It was observed that rutile nanorods exhibited a photoelectric conversion efficiency (PCE) of 4.28% compared to that of commercial Degussa P25 TiO_2 (PCE = 3.95%). It may be due to the unidirectional electron transport induced by the rod nature without suffering from grain boundaries compared to P25 nanoparticles irrespective of its anatase/rutile crystal phase. The rutile rod structure exhibited higher V_{OC} of 0.82 V which is quite impressive in the case of rutile TiO_2-based DSSC devices.[51] During PANI insertion the photocurrent density was significantly improved for both P25 (J_{SC}: 12.63 mA/cm^2) and rutile TiO_2 (J_{SC}: 14.73 mA/cm^2). Furthermore, PANI-coated TiO_2 rod based photoanodes exhibited an overall PCE of 6.23% with a significant improvement of J_{SC} of the DSSC device (∼62%). This result interprets that PANI helps to accelerate faster electron mobility and shorter charge recombination of the photoanode leading to enhanced efficiency. On the contrary, PANI insertion causes reduction in fill factor to 0.56 from 0.63 which may be due to the reduction of the TiO_2 surface area that is inaccessible for the dye sensitization, causing steric constraints, and defective PANI molecule accumulation on the surfaces of TiO_2 rod leads

DOI: 10.1021/acsomega.8b02628
ACS Omega 2019, 4, 1130−1138

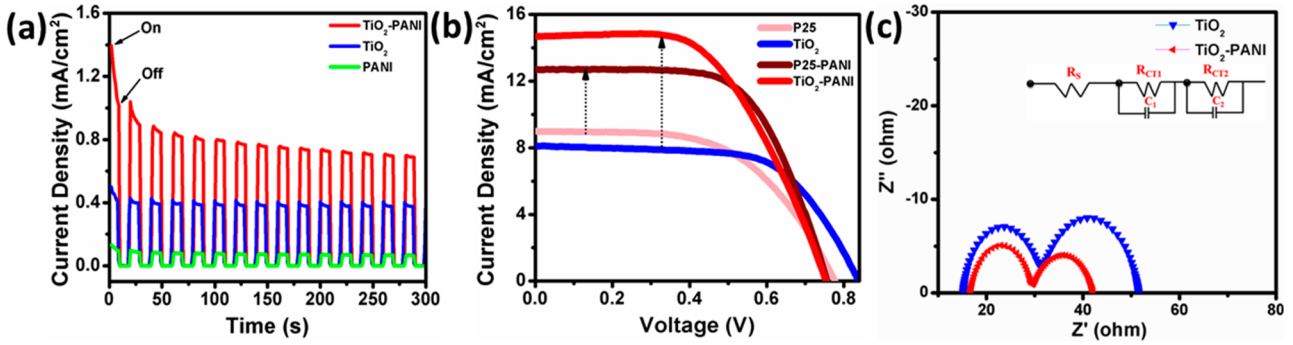

Figure 7. (a) Transient photocurrent response curve for PANI, TiO_2, and TiO_2–PANI film and (b) *J*–*V* characteristic plot of Degussa P25, P25–PANI composite, synthesized rutile TiO_2, and rutile TiO_2–PANI composite DSSC devices and (c) Nyquist plots of N719 dye-sensitized TiO_2 and TiO_2–PANI photoanodes (inset: corresponding equivalent circuit used for fitting).

Table 1. Photovoltaic Parameters of Commercial Degussa P25 TiO_2, P25–PANI, Synthesized TiO_2 Rutile Nanorod, and PANI Composite Based DSSC Devices

sample	J_{SC} (mA/cm^2)	V_{OC} (V)	FF	PCE ± 0.2 (%)
P25	8.99	0.77	0.56	3.95
P25–PANI	12.63	0.76	0.57	5.37
TiO_2	8.10	0.84	0.63	4.28
TiO_2–PANI	14.73	0.76	0.56	6.23

to recombination of photoexcited carriers at higher content of PANI than optimal conditions.

To understand the charge transport in the DSSC interfaces, electrochemical impedance spectroscopic studies were performed for TiO_2 and PANI–TiO_2 devices. The series resistance (R_S) represents the lower frequency intercepts on the real axis. Besides, the second high frequency semicircle represents the charge transfer resistance originated from the TiO_2/N719 dye/I^-–I_3^- electrolyte interface (R_{CT2}).[5,8] As the counter (Pt) and electrolyte (I^-/I_3^-) used the same for both the samples, our interest was to study the R_{CT2} interface zone for both the devices. Figure 7c shows the impedance spectra (Nyquist plot) and corresponding equivalent circuit diagram (inset) of cells for TiO_2 and TiO_2–PANI devices recorded from 10^{-2} to 10^6 Hz, consisting of only two semicircles. As shown in Figure 7c, both the devices exhibit close values of R_S, 15.36 Ω for bare TiO_2 and 14.58 Ω for TiO_2–PANI devices, respectively, which is due to the use of the same Pt counter electrodes and I^-/I_3^- electrolyte in all the devices. Importantly, the charge transfer resistances, R_{CT1} and R_{CT2} of 21.08 Ω and 31.47 Ω, for the TiO_2–PANI device are lower than 23.13 Ω and 36.62 Ω for bare TiO_2 devices, respectively. This indicates that the PANI-layered nanorod exhibits lower charge transport resistance than bare TiO_2, which leads to minimizing of the charge recombination and lowering of the interfacial resistance and therefore better solar cell performance. However, maximum J_{SC} (14.73 mA/cm^2) observed for the composite-based device indicates that deposition of PANI successfully overruled the reduced surface area related factor by working as an electron transportation layer onto rutile nanorods along with its electrochromic performance to boost up the photovoltaic efficiency of the rutile nanorods. Previously, Zhu et al. (2012) demonstrated PANI-hybridized ZnO photoanode in DSSC with 60% enhanced efficiency for the hybridized photoanode.[41] As an influence from that report, we have explored the same mechanism with rutile TiO_2 which also exhibits enhanced efficiency on PANI insertion on hybridization to the DSSC performance. Comparative photovoltaic performance of 1D rutile TiO_2-based cells in DSSCs has been summarized in Table 2.

The increase of photocurrent density can be mainly explained by considering the hybrid effect between TiO_2 and PANI as it may induce the high efficiency of charge separation. Once the dye absorbs the light and generates photoexcited

Table 2. Comparative Photovoltaic Performance of N719 Dye-Sensitized 1D Rutile TiO_2-Based Cells in DSSCs[a]

photoanode	V_{OC} (V)	J_{SC} (mA/cm^2)	FF	PCE (%)	reference
NW	0.758	10.24	0.56	4.35	22
NW	0.7	6.25	0.58	2.6	23
NR	0.78	6.95	0.68	3.68	24
NR, $TiCl_4$-treated NR	0.70, 0.76	7.31, 12.24	0.73, 0.66	3.76, 6.31	25
NW, $TiCl_4$-treated NW	0.54, 0.58	4.8, 8.7	0.41, 0.42	1.2, 2.9	26
NR	0.69	11.24	0.62	4.87	27
TiO_2 NRs, etched TiO_2 NRs	0.77, 0.77	4.29, 11.55	0.40, 0.60	1.30, 5.36	29
NR	0.76	1.47	0.46	0.52	30
NR, 7 h etched NR	0.79, 0.71	5.88, 20.49	0.51, 0.54	2.35, 7.91	31
NR	0.63	2.57	0.47	0.76	32
NR	0.71	6.05	0.70	3.0	38
NR microsphere	0.719	6.8	0.60	2.92	47
NRs, Au NP on NR	0.67, 0.63	1.07, 2.57	0.43, 0.56	0.31, 0.94	48
NR, PANI-layered NR	0.84, 0.76	8.104, 14.73	0.63, 0.56	4.28, 6.23	present work

[a]NR: nanorod; NW: nanowire; NP: nanoparticle; h: hours; PANI: polyaniline.

DOI: 10.1021/acsomega.8b02628
ACS Omega 2019, 4, 1130–1138

electrons, the hybridized PANI layer may promptly conduct them into the conduction band of TiO_2, resulting in increasing the electron density on the conduction band of TiO_2. Furthermore, PANI appears like a blanket on the entire bundle of rods rather than coating individual rods. Also, it does not influence the morphology or the nature of the rutile rod distribution and their arrangement. On the basis of photocurrent measurements, we project PANI-wrapped rutile TiO_2 nanorods as a new type of modified photoanode material. Comparative photovoltaic performance of 1D rutile TiO_2-based cells in DSSCs has been summarized in Table 2. The characteristics of the electron-transporting layer, carrier mobility, energy band alignment, morphology, trap states, and related interfacial properties are major factors to determine the device behavior and photovoltaic performance of oxide in a solar cell.[52,53]

CONCLUSION

Highly crystalline rutile nanorods synthesized by a low-temperature hydrothermal technique wrapped with PANI were explored as alternative photoanode in a DSSC device which exhibited the photoelectric conversion efficiency (PCE) of 4.28% and a high V_{OC} of 0.82 V. Furthermore, *in situ* deposition of polyaniline (PANI) as an electron-transporting layer onto the surface of nanorods boosts up the photovoltaic efficiency of the rutile nanorods to 6.23%. Various physicochemical characterizations established successful deposition of PANI layers on the TiO_2 nanorod. The photoelectrochemical study also confirms that on illumination PANI enhances the rate of electron conduction of TiO_2 compared to the respective bare forms. Improving the charge transport on deposition of the PANI layer over the nanorod surface may open up a new avenue for improving the efficiency of DSSC devices besides conventional $TiCl_4$ treatment or other conventional scattering layer deposition.

EXPERIMENTAL SECTION

Materials. Titanium tetra-isopropoxide ($[Ti(OCHMe_2)_4]$ 97%, TTIP, AR) and ammonium persulfate ($[NH_4]_2S_2O_8$) were purchased from Sigma-Aldrich. Aniline and hydrochloric acid (37% HCl, EMPARTA) were purchased from Merck Ltd., India, and used without further purification.

Synthesis of Rutile TiO_2 Nanorods. TiO_2 nanorods were synthesized using aqueous solution of 1.7 mmol of TTIP under vigorous stirring for ∼2 h followed by 1 h aging at room temperature. Concentrated HCl was added proportionately to keep the solution pH ≤ 1.5. The whole mixture was transferred into a 45 mL Teflon-lined stainless steel autoclave, sealed, and heated at 160 °C for 5 h and then cooled to room temperature. The obtained mixture was collected and centrifuged at ∼11 000 rpm followed by washing with water and ethanol for several times. Subsequently, the resultant white product was dried at 120 °C in a vacuum oven.

Fabrication of TiO_2 Film. The TiO_2 films were fabricated by the doctor blading method on fluorine-doped tin oxide (FTO) (7 Ω/cm^2) glass substrate using a homemade paste of TiO_2 with ethyl cellulose and α-terpinol (Sigma-Aldrich).We used three layers of TiO_2 paste to fabricate the TiO_2 photoanode followed by annealing at 450 °C for 30 min.

Deposition of the Polyaniline (PANI) Layer on TiO_2 Film. PANI was allowed to deposit *in situ* onto the TiO_2 film surface. In detail, 3.24 mL of aniline hydrochloride solution (0.1 M) and 10 mL of HCl solution (0.1 M) were mixed in a reaction vessel placed in an ice bath (0−5 °C), and the mixture was stirred thoroughly to obtain a uniform suspension. Next, the nonconducting side of the fabricated film was masked with scotch tape and further dipped inside the solution. An amount of 3.24 mL of ammonium persulfate solution (0.1 M) was dropwise added to the mixture over 1 h. Further, the solution was allowed to react in an ice bath for another 2 h. The solution color changed to green accompanied by a green layer deposition over the TiO_2 film, visually indicating PANI formation. After that, the film was removed from the solution and repeatedly washed with water until the pH value was adjusted to ∼7. Finally, the PANI-deposited TiO_2 film was completely dried under an IR lamp for further use.

Material Characterization. The phase evaluation and purity of the synthesized TiO_2 and TiO_2−PANI composite samples were analyzed by X-ray diffraction measurements on an X'pert pro MPD XRD of PANalytical system with Cu Kα radiation (λ = 1.5406 Å). The morphology evaluation and crystallinity nature of synthesized TiO_2 and TiO_2−PANI composite samples were recorded through bright-field image, high-resolution transmission electron microscopy (HRTEM) image, and fast Fourier transform (FFT) pattern using a Tecnai G2 30ST (FEI) Ultra High Resolution Transmission Electron Microscope operating at 200 kV. A PerkinElmer, Spectrum two FT-IR spectrometer (with a resolution of 4 cm^{-1}) was used for the Fourier transformed-infrared (FT-IR) measurement using potassium bromide (FTIR grade ≥99%, Sigma-Aldrich). Raman spectroscopic measurement has been performed on a STR500 (Cornes Technologies system by using 514.5 nm Ar^+ green laser with 50 mW power). The surface and cross-sectional image of bare TiO_2 and TiO_2−PANI composite films were recorded using field emission scanning electron microscopy on a Supra 35VP (Carl Zeiss) Field Emission Scanning Electron Microscope (FESEM) operating at 20 kV. The surface area of both the samples was obtained using the nitrogen physisorption measurements and the Brunauer−Emmet−Teller (BET) method within the relative pressure (p/p_0) range of 0.05−0.20, and the pore size distribution was calculated by the Barret−Joyner−Halenda (BJH) method using the Quantachrome (iQ3) instrument after evacuation at 150 °C for 4 h. The UV absorption spectra and diffused reflectance spectra were recorded on a UV−vis−NIR spectrophotometer (Shimadzu UV-3600). X-ray photoemission spectroscopy (XPS) measurements were performed in a PHI 5000 Versa probe II scanning XPS microprobe (ULVAC-PHI, U.S.) at room temperature acquired with monochromatic Al K_α ($h\nu$ = 1486.6 eV) radiation with a total resolution of about 0.7 eV and a beam size of 100 μm.

Fabrication of DSSC. For device fabrication, each film thickness was maintained at ∼8 μm with an active area of 0.2826 cm^2. The films were soaked in ethanolic solution of N719 dye (0.5 mM, Solaronix) for a period of 24 h. For electrolyte preparation, 0.3 M 1-methylbenzimidazole (NMB) was thoroughly mixed with 1:1 volume ratio acetonitrile and 3-methoxypropionitrile (MPN) solution followed by the addition of 0.4 M LiI, 0.4 M tetrabutylammonium iodide (TBAI), and 0.04 M I_2. The entire mixture was stirred overnight. Pt solutions (Platisol T, BN 40/170311FM, Solaronix, Switzerland) having Pt particles in the size range of 10−20 nm were drop casted on a cleaned FTO glass. The deposited layer was gradually air-dried followed by heating at 450 °C for 15 min, in order to activate the platinum layer for

DOI: 10.1021/acsomega.8b02628
ACS Omega 2019, 4, 1130−1138

working. Finally, the prepared I_3^-/I^- liquid electrolyte was infiltrated into the photoanode cell and made a sandwiched DSSC device with the Pt counter electrode. Sandwich-type DSSCs were then assembled using the dye-adsorbed TiO_2 film and a Pt electrode with a hot-melt film (~25 μm, Surlyn, Dyesol) between them. The photovoltaic performances of the assembled devices were measured under 1000 W/m^2 of light from a Wacom AAA continuous solar simulator (model: WXS-210S-20, AM1.5G). The $I-V$ characteristic of the device was recorded using an EKO MP-160i $I-V$ Tracer. The presented data are average measurements done on two different devices for each sample. Electrochemical impedance spectroscopy (EIS) measurements were performed by using an Autolab PGSTAT 10 and a frequency response analyzer (FRA) module with the frequency range from 0.1 Hz to 100 kHz. The devices were measured at the 0.84 V open-circuit voltage for bare TiO_2 and 0.76 V open-circuit voltage for TiO_2–PANI devices. The data were further fitted using Z-view software (version 3.4d, Scribner Associates, Inc., USA).

■ ASSOCIATED CONTENT

Supporting Information

The Supporting Information is available free of charge on the ACS Publications website at DOI: 10.1021/acsomega.8b02628.

Table of comparative study of surface characteristics and dye loading properties for TiO_2 and TiO_2–PANI samples (PDF)

■ AUTHOR INFORMATION

Corresponding Author

E-mail: psujathadevi@cgcri.res.in, psujathadevi@gmail.com. Tel.: 033-2322-3487. Fax: +91-33-24730957.

ORCID

Anurag Roy: 0000-0002-2097-9442
Soumita Mukhopadhyay: 0000-0001-7919-1214
Parukuttyamma Sujatha Devi: 0000-0002-6224-7821
Senthilarasu Sundaram: 0000-0001-8190-3786

Present Address

[§]School of Materials Sciences, Indian Association for the Cultivation of Science, Kolkata 700032, India.

Author Contributions

[#]A.R. and S.M. contributed equally

Notes

The authors declare no competing financial interest.

■ ACKNOWLEDGMENTS

A.R. acknowledges the INSPIRE program of Department of Science and Technology (DST) Government of India for fellowship. A.R. also acknowledges the Newton-Bhabha Ph.D Program of 2016–2017 jointly funded by DST and British Council. S.M. is indebted to the University Grant Commission (UGC), Government of India, for the fellowship to carry out the Ph.D program. P.S.D. acknowledges the Ministry of New and Renewable Energy (MNRE) for financial support under the CSIR-TAPSUN program, GAP-0339.

■ REFERENCES

(1) Kapilashrami, M.; Zhang, Y.; Liu, Y.-S.; Hagfeldt, A.; Guo, J. Probing the optical property and electronic structure of TiO_2 nanomaterials for renewable energy applications. *Chem. Rev.* **2014**, *114*, 9662–9707.

(2) Sang, L.; Zhao, Y.; Burda, C. TiO_2 nanoparticles as functional building blocks. *Chem. Rev.* **2014**, *114*, 9283–9318.

(3) Ronca, E.; Pastore, M.; Belpassi, L.; Tarantelli, F. Influence of the dye molecular structure on the TiO_2 Conduction band in dye-sensitized solar cells: disentangling charge transfer and electrostatic effects. *Energy Environ. Sci.* **2013**, *6*, 183–193.

(4) O'regan, B.; Grätzel, M. A low-cost, high-efficiency solar cell based on dye-sensitized colloidal TiO_2 films. *Nature* **1991**, *353*, 737–740.

(5) Das, P. P.; Agarkar, S. A.; Mukhopadhyay, S.; Manju, U.; Ogale, S. B.; Devi, P. S. defects in chemically synthesized and thermally processed ZnO nanorods: implications for active layer properties in dye-sensitized solar cells. *Inorg. Chem.* **2014**, *53*, 3961–3972.

(6) Pratim Das, P.; Roy, A.; Das, S.; Devi, P. S. Enhanced stability of Zn_2SnO_4 with N719, N3 and eosin Y dye molecules for DSSC application. *Phys. Chem. Chem. Phys.* **2016**, *18*, 1429–1438.

(7) Das, P. P.; Roy, A.; Devi, P. S. Zn_2SnO_4 as an alternative photoanode for dye sensitized solar cells: current status and future scopes. *Trans. Indian Ceram. Soc.* **2016**, *75*, 147–154.

(8) Roy, A.; Das, P. P.; Selvaraj, P.; Sundaram, S.; Devi, P. S. Perforated $BaSnO_3$ nanorods exhibiting enhanced efficiency in dye sensitized solar cells. *ACS Sustainable Chem. Eng.* **2018**, *6*, 3299–3310.

(9) Shao, F.; Sun, J.; Gao, L.; Yang, S.; Luo, J. Growth of various TiO_2 nanostructures for dye-sensitized solar cells. *J. Phys. Chem. C* **2011**, *115*, 1819–1823.

(10) Yan, X.; Feng, L.; Jia, J.; Zhou, X.; Lin, Y. Controllable synthesis of anatase TiO_2 crystals for high-performance dye-sensitized solar cells. *J. Mater. Chem. A* **2013**, *1*, 5347–5352.

(11) Manseki, K.; Kondo, Y.; Ban, T.; Sugiura, T.; Yoshida, T. Size-controlled synthesis of anisotropic TiO_2 single nanocrystals using microwave irradiation and their application for dye-sensitized solar cells. *Dalton Trans.* **2013**, *42*, 3295–3299.

(12) Zhang, W.; Xie, Y.; Xiong, D.; Zeng, X.; Li, Z.; Wang, M.; Cheng, Y.-B.; Chen, W.; Yan, K.; Yang, S. TiO_2 Nanorods: A facile size- and shape-tunable synthesis and effective improvement of charge collection kinetics for dye- sensitized solar cells. *ACS Appl. Mater. Interfaces* **2014**, *6*, 9698–9704.

(13) Liao, J.-Y.; He, J.-W.; Xu, H.; Kuang, D.-B.; Su, C.-Y. Effect of TiO_2 morphology on photovoltaic performance of dye-sensitized solar cells: nanoparticles, nanofibers, hierarchical spheres and ellipsoid spheres. *J. Mater. Chem.* **2012**, *22*, 7910–7918.

(14) Mukhopadhyay, S.; Maiti, D.; Saha, A.; Devi, P. S. Shape transition of TiO_2 nanocube to nanospindle embedded on reduced graphene oxide with enhanced photocatalytic activity. *Cryst. Growth Des.* **2016**, *16*, 6922–6932.

(15) Hoffmann, M. R.; Martin, S. T.; Choi, W.; Bahnemann, D. W. Environmental applications of semiconductor photocatalysis. *Chem. Rev.* **1995**, *95*, 69–96.

(16) Schneider, J.; Matsuoka, M.; Takeuchi, M.; Zhang, J.; Horiuchi, Y.; Anpo, M.; Bahnemann, D. W. Understanding TiO_2 photocatalysis: mechanisms and materials. *Chem. Rev.* **2014**, *114*, 9919–9986.

(17) Scanlon, D. O.; Dunnill, C. W.; Buckeridge, J.; Shevlin, S. A.; Logsdail, A. J.; Woodley, S. M.; Catlow, C. R. A.; Powell, J.; Palgrave, R. G.; Parkin, I. P.; Watson, G. W.; Keal, T. W.; Sherwood, P.; Walsh, A.; Sokol, A. A. Band alignment of rutile and anatase TiO_2. *Nat. Mater.* **2013**, *12*, 798–801.

(18) Nosaka, Y.; Mosaka, A. Y. Reconsideration of intrinsic band alignments within anatase and rutile TiO_2. *J. Phys. Chem. Lett.* **2016**, *7*, 431–434.

(19) Park, N. G.; van de Lagemaat, J.; Frank, A. J. Comparison of dye-sensitized rutile- and anatase-based TiO_2 solar cells. *J. Phys. Chem. B* **2000**, *104*, 8989–8994.

(20) Wang, Y. W.; Zhang, L. Z.; Deng, K. J.; Chen, X. Y.; Zou, Z. G. Low temperature synthesis and photocatalytic activity of rutile TiO_2 nanorod superstructures. *J. Phys. Chem. C* **2007**, *111*, 2709–2714.

DOI: 10.1021/acsomega.8b02628
ACS Omega 2019, 4, 1130–1138

(21) Hosono, E.; Fujihara, S.; Kakiuchi, K.; Imai, H. Growth of Submicrometer-Scale Rectangular parallelepiped rutile TiO_2 films in aqueous $TiCl_3$ solutions under hydrothermal conditions. *J. Am. Chem. Soc.* **2004**, *126*, 7790−7791.
(22) Feng, X. J.; Shankar, K.; Varghese, O. K.; Paulose, M.; Latempa, T. J.; Grimes, C. A. Vertically aligned single crystal TiO_2 nanowire arrays grown directly on transparent conducting oxide coated glass: synthesis details and applications. *Nano Lett.* **2008**, *8*, 3781−3786.
(23) Oh, J.-K.; Lee, J.-K.; Kim, H.-S.; Han, S.-B.; Park, K.-W. TiO_2 branched nanostructure electrodes synthesized by seeding method for dye-sensitized solar cells. *Chem. Mater.* **2010**, *22*, 1114−1118.
(24) Feng, X.; Zhu, K.; Frank, A. J.; Grimes, C. A.; Mallouk, T. E. Rapid charge transport in dye-sensitized solar cells made from vertically aligned single-crystal rutile TiO_2 nanowires. *Angew. Chem., Int. Ed.* **2012**, *51*, 2727−2730.
(25) Yu, H.; Pan, J.; Bai, Y.; Zong, X.; Li, X.; Wang, L. Hydrothermal synthesis of a crystalline rutile TiO_2 nanorod based network for efficient dye-sensitized solar cells. *Chem. - Eur. J.* **2013**, *19*, 13569−13574.
(26) Kumar, A.; Madaria, A. R.; Zhou, C. Growth of aligned single-crystalline rutile TiO_2 nanowires on arbitrary substrates and their application in dye-sensitized solar cells. *J. Phys. Chem. C* **2010**, *114*, 7787−7792.
(27) Mali, S. S.; Betty, C. A.; Bhosale, P. N.; Patil, P. S.; Hong, C. K. From nanocorals to nanorods to nanoflowers nanoarchitecture for efficient dye-sensitized solar cells at relatively low film thickness: all hydrothermal process. *Sci. Rep.* **2015**, *4*, 1−8.
(28) Enache-Pommer, E.; Liu, B.; Aydil, E. S. Electron Transport and recombination in dye-sensitized solar cells made from single-crystal rutile TiO_2 nanowires. *Phys. Chem. Chem. Phys.* **2009**, *11*, 9648−9652.
(29) Lv, M.; Zheng, D.; Ye, M.; Sun, L.; Xiao, J.; Guo, W.; Lin, C. Densely aligned rutile TiO_2 nanorod arrays with high surface area for efficient dye-sensitized solar cells. *Nanoscale* **2012**, *4*, 5872−5879.
(30) Wang, S.-M.; Dong, W.-W.; Tao, R.-H.; Deng, Z.-H.; Shao, J.-Z.; Hu, L.-H. Optimization of single-crystal rutile TiO_2 nanorod arrays based dye-sensitized solar cells and their electron transport properties. *J. Power Sources* **2013**, *235*, 193−201.
(31) Lv, M.; Zheng, D.; Ye, M.; Xiao, J.; Guo, W.; Lai, Y.; Sun, L.; Lin, C.; Zuo, J. Optimized porous rutile TiO_2 nanorod arrays for enhancing the efficiency of dye-sensitized solar cells. *Energy Environ. Sci.* **2013**, *6*, 1615−1622.
(32) Guo, W.; Xu, C.; Wang, X.; Wang, S.; Pan, C.; Lin, C.; Wang, Z. L. Rectangular bunched rutile TiO_2 nanorod arrays grown on carbon fiber for dye-sensitized solar cells. *J. Am. Chem. Soc.* **2012**, *134*, 4437−4441.
(33) Ge, M.; Cao, C.; Huang, J.; Li, S.; Chen, Z.; Zhang, K.-Q.; Al-Deyabd, S. S.; Lai, Y. A Review of one-dimensional TiO_2 nanostructured materials for environmental and energy applications. *J. Mater. Chem. A* **2016**, *4*, 6772−6801.
(34) Lan, C.-M.; Liu, S.-E.; Shiu, J.-W.; Hu, J.-Y.; Lin, M.-H.; Diau, E. Formation of size-tunable dandelion-like hierarchical rutile titania nanospheres for dye-sensitized solar cells. *RSC Adv.* **2013**, *3*, 559−565.
(35) Das, P. P.; Mukhopadhyay, S.; Agarkar, S. A.; Jana, A.; Devi, P. S. Photochemical performance of ZnO nanostructures in dye sensitized solar cells. *Solid State Sci.* **2015**, *48*, 237−243.
(36) Das, P. P.; Roy, A.; Tathavadekar, M.; Devi, P. S. Photovoltaic and photocatalytic performance of electrospun Zn_2SnO_4 hollow fibers. *Appl. Catal., B* **2017**, *203*, 692−703.
(37) Roy, A.; Selvaraj, P.; Devi, P. S.; Sundaram, S. Morphology tuned $BaSnO_3$ active layer for ambient perovskite solar cells. *Mater. Lett.* **2018**, *219*, 166−169.
(38) Liu, B.; Aydil, E. S. Growth of oriented single-crystalline rutile TiO_2 nanorods on transparent conducting substrates for dye-sensitized solar cells. *J. Am. Chem. Soc.* **2009**, *131*, 3985−3990.
(39) Maity, N.; Kuila, A.; Das, S.; Mandal, D.; Shit, A.; Nandi, A. K. Optoelectronic and photovoltaic properties of graphene quantum dot-polyanilines nanostructures. *J. Mater. Chem. A* **2015**, *3*, 20736−20748.
(40) Zhu, J.; Huo, X.; Liu, X.; Ju, H. Gold nanoparticles deposited polyanilines-TiO_2 nanotube for surface plasmon resonance enhanced photoelectrochemical biosensing. *ACS Appl. Mater. Interfaces* **2016**, *8*, 341−349.
(41) Zhu, S.; Wei, W.; Chen, X.; Jiang, M.; Zhou, Z. Hybrid structure of polyaniline/ZnO nanograss and its application in dye-sensitized solar cell with performance improvement. *J. Solid State Chem.* **2012**, *190*, 174−179.
(42) Lee, K.; Cho, S.; Kim, M.; Kim, J.; Ryu, J.; Shin, K.-Y.; Jang, J. Highly porous nanostructured polyaniline/carbon nanodots as efficient counter electrodes for Pt-free dye-sensitized solar cells. *J. Mater. Chem. A* **2015**, *3*, 19018−19026.
(43) Jeon, S. S.; Kim, C.; Lee, T. H.; Lee, Y. W.; Do, K.; Ko, J.; Im, S. S. Camphorsulfonic Acid-Doped polyaniline transparent counter electrode for dye-sensitized solar cells. *J. Phys. Chem. C* **2012**, *116*, 22743−22748.
(44) Cho, S.; Hwang, S. H.; Kim, C.; Jang, J. Polyaniline porous counter-electrodes for high performance dye-sensitized solar cells. *J. Mater. Chem.* **2012**, *22*, 12164−12171.
(45) Zhang, H.; Zong, R.; Zhu, Y. Photocorrosion inhibition and photoactivity enhancement for zinc oxide via hybridization with monolayer polyaniline. *J. Phys. Chem. C* **2009**, *113*, 4605−4611.
(46) Wang, Y.; Xu, J.; Zong, W.; Zhu, Y. Enhancement of photoelectric catalytic activity of TiO_2 film via polyaniline hybridization. *J. Solid State Chem.* **2011**, *184*, 1433−1438.
(47) Rui, Y.; Li, Y.; Zhang, Q.; Wang, H. Facile Synthesis of rutile TiO_2 nanorod microspheres for enhancing light-harvesting of dye-sensitized solar cells. *CrystEngComm* **2013**, *15*, 1651−1656.
(48) Ghaffari, M.; Cosar, M. B.; Yavuz, H. I.; Ozenbas, M.; Okyay, A. K. Effect of Au nano-particles on TiO_2 nanorod electrode in dye-sensitized solar cells. *Electrochim. Acta* **2012**, *76*, 446−452.
(49) Waghmode, B. J.; Soni, R.; Patil, K. R.; Malkhede, D. D. Calixarene based nanocomposite materials for high-performance supercapacitor electrode. *New J. Chem.* **2017**, *41*, 9752−9761.
(50) Parveen, N.; Ansari, M. O.; Han, T. H.; Cho, M. H. Simple and rapid synthesis of ternary polyaniline/titanium oxide/graphene by simultaneous TiO_2 generation and aniline oxidation as hybrid materials for supercapacitor applications. *J. Solid State Electrochem.* **2017**, *21*, 57−68.
(51) Feng, X.; Shankar, K.; Paulose, M.; Grimes, C. A. Tantalum-doped titanium dioxide nanowire arrays for dye sensitized solar cells with high open-circuit voltage. *Angew. Chem.* **2009**, *121*, 8239−8242.
(52) Wei, A.; Zuo, Z.; Liu, J.; Lin, K.; Zhao, Y. Transport and interfacial transfer of electrons in dye-sensitized solar cells based on a TiO_2 nanoparticle/TiO_2 nanowire "double-layer" working electrode. *J. Renewable Sustainable Energy* **2013**, *5*, No. 033101.
(53) Chandiran, A. K.; Abdi-Jalebi, M.; Nazeeruddin, M. K.; Grätzel, M. Analysis of electron transfer properties of ZnO and TiO_2 photoanodes for dye-sensitized solar cells. *ACS Nano* **2014**, *8*, 2261−2268.

DOI: 10.1021/acsomega.8b02628
ACS Omega 2019, 4, 1130−1138